Computational Modeling of Anisotropic Engineered Heart Tissue

By

Yifei Bai

B.A., Tongji University, 2018

Thesis

Submitted in partial fulfillment of the requirements for the

Degree of Master of Science in the School of Engineering at Brown University

PROVIDENCE, RHODE ISLAND

MAY 2020

This thesis by Yifei Bai is accepted in its present form by the Department of Engineering as satisfying the thesis requirements for the degree of Master of Science

Date 04/30/2020

Vikas Srivastava, Advisor

Approved by the Graduate Council

Date _____

Andrew G. Campbell, Dean of the Graduate School

Preface and acknowledgements

I have received a great deal of support and assistant throughout this project. I would like to thank my supervisor, Professor Vikas Srivastava first. He has always been supportive to me whenever I am stuck with some problems and provided his encouragements and advice. Now I have been away from Providence for almost a year, I really miss those time when I can go upstairs and have a discussion with him about my research.

Thanks to Dr. Nicholas Kaiser and Professor Kareen Coulombe, their extraordinary experimental work inspired me in many ways. In the several meetings we had in the past two years, they were always patient to my naïve questions.

I also want to thank my “desk mate”, Sijun Niu. There are so many memories, after all, we are the first two members of the lab. One image is still fresh now, that is, in many weekends where there were just me and him working in the corner of the ERC building and eating countless subway sandwiches. He offered me great help when I came to Providence for the first time. Thanks to Savan Santoki and Luis Marquez, hanging out with them is one of the most delightful memories I had in the United States.

ABSTRACT

Cardiac patch therapies have become a promising treatment to lower the risk of heart failure after myocardial infarct to restore heart function. Engineered tissue scaffolds with microarchitecture are designed to construct cardiac patches which have similar mechanical properties to native myocardium. We studied the effect of composite architecture on the overall response of the engineered tissue scaffold patch using three-dimensional finite element models constructed in Abaqus. Ogden nonlinear hyperelastic model and Neo-Hookean model were selected to represent the soft matrix and the stiff fibers respectively. The model parameters were calibrated using Coulombe Lab's uniaxial tension test data on these materials. Longitudinal and transverse tension simulations are then implemented to find the mechanical behavior of the composite to study anisotropy and the effect of various microarchitectural design parameters, including fiber distance and angle. We have also developed a nonlinear hyperelastic continuum constitutive model to efficiently simulate the anisotropic response of engineered tissue scaffolds patch on three-dimensional heart geometry.

Table of Contents

Preface and acknowledgements ..... **iii**

ABSTRACT ..... **iv**

Table of Contents ..... **v**

List of Illustrations ..... **vii**

Chapter 1. Introduction **1**

1.1 Background **1**

1.2 Physiology **2**

1.2.1 Heart Structure **2**

1.2.2 Cardiac Muscle **3**

1.2.3 Cardiac Cycle **5**

1.2.4 Myocardial Infarction **7**

1.2.5 Cardiac Patch **9**

1.3 Problem Description **10**

Chapter 2. Computational Modeling **12**

2.1 Microstructure based finite element model **12**

2.1.1 Basic steps for finite element analysis **12**

2.1.2 Creating the geometry **12**

2.1.3 Obtaining material properties of the collagen fiber and matrix **14**

2.1.4 Generate mesh and assign material properties **15**

2.1.5 Apply load and boundary conditions **16**

2.1.6 Results and post analyses **17**

2.2 Parametric Study **20**

2.2.1 Effect of angle variation **20**

2.2.2 Effect of fiber distance **21**

2.2.3 Anisotropy analysis **22**

Chapter 3. Continuum Scale Constitutive modeling **24**

3.1 Essential elements of continuum mechanics **24**

3.2 Modification of the Holzapfel model 25

Chapter 4. Conclusion and Discussion 30

Bibliography 33

List of Illustrations

Figure 1.1 Structure of the heart and the course of blood flow through the heart chambers and heart valves…….. 3

Figure 1.2 (a) Histology of cardiac muscle **(b)** Schematic of muscle fibers across the ventricle wall…… …… .. 4

Figure 1.3 Events of the cardiac cycle for left ventricular function…….. .7

Figure 1.4 Pathogenesis of long-term heart failure…… 8

Figure 2.1 Procedure of creating the geometry: (a) Create a solid block; (b) Partition face by sketch; (c) Partition body by extruding…… …… 14

Figure 2.2 Stress-Stretch Curve of Experiments and Model Fits of (a)Matrix (b) Fiber …….. 15

Table 2.1 Material Parameters for Matrix and Fiber Material…… …. 15

Figure 2.3 Meshed composite in Hypermesh 2019…… …….. 16

Table 2.2 Boundary conditions for node sets…… …. . .16

Figure 2.4 Mises stress (MPa) contour plots for longitudinal tensile simulation: (a) deformed composite; (b) deformed fibers…… … … 17

Figure 2.5 Post analysis of longitudinal tensile simulation (a) Fiber distance vs composite stretch; (b) Fiber angle vs composite stretch…… … 18

Figure 2.6 Mises stress (MPa) contour plots for transverse tensile simulation: (a) side view; (b) top view…… …… … 19

Figure 2.7 Post analysis of transverse tensile simulation (a) Fiber distance vs composite stretch; (b) Fiber angle vs composite stretch…… …… …….19

Table 2.1 Values defined for parametric study…… …… ….20

Figure 2.8 Stress-stretch curves for composites with different fiber angles: (a) longitudinal; (b) transverse……... 21

Figure 2.9 Stress-stretch curves for composites with different fiber distances: (a)

longitudinal; (b) transverse……... 22

Figure 2.10 Anisotropy ratios of native cardiac tissue and some configurations of the engineered tissue with the effect of (a) fiber angle difference (b) fiber distance difference…… ……. . 23

Figure 3.1 Schematic of a rectangular tissue scaffold with two symmetrically arranged families of fibers……... 29

Figure 3.2 Stress-stretch curve for the proposed model and simulation result (a) longitudinal (b) transverse…… 29

Table 3.1 Parameters used in the constitutive model……... 29

Figure 4.1 Principal strain for the infarcted heart with implanted patch……. 31

Figure 4.2 Principal strain for the infarcted heart without implanted patch…… 32

Chapter 1. Introduction

1.1 Background

Cardiovascular disease (CVD) has caused 17.9 million deaths, accounting for 44% among all the noncommunicable diseases (World Health Organization, 2018). Apart from catastrophic acute myocardial infarcts, different postinfarct mechanisms, including infarct expanding, ventricular remodeling, and coupling of infarct and healthy myocardium, may also influence cardiac function on a larger time scale (Holmes, Borg, and Covell 2005). Postinfarct ventricular remodeling is already considered to be a compensatory mechanism of congestive cardiac failure (Fujimoto et al. 2007). Although long-term use of angiotensin-converting enzyme inhibitors and beta-blockers have been proven beneficial in congestive heart failure (Bahit, Kochar, and Granger 2018), the function of the infarcted heart is not restored, and the financial cost of this therapy is a massive burden for the patients (Fujimoto et al. 2007). The most direct way to restore the contracting capability is to inject cardiac myocytes to the infarcted area. However, the survival rate of the injected cells is relatively low. Besides, immature cells could be washed out by the cardiac vasculature and carried to other organs. This phenomenon may result in infarction in healthy tissue and even teratoma (Dow et al. 2005).

In contrast to injecting isolated cells, transplanting an engineered cardiac patch is an attractive approach to solve this problem. Eschenhagen et al. (Eschenhagen et al. 1997) are

among the first ones to use hydrogel in cardiac tissue engineering. They developed a three-dimensional engineered tissue to observe in vitro isometric contraction. The idea of the cardiac patch is brought out by Shimizu (Shimizu et al. 2002); they created a 3-dimensional engineered tissue with four layers of cell sheets. However, this type of engineered tissue graft is so fragile that it cannot provide the required mechanical property in the heart cycle. It is widely accepted that the design of engineered cardiac tissue should match material properties of the surrounding healthy host tissue, such as stiffness, anisotropy, and tensile strength (Kaiser and Coulombe 2015). Kaiser et al. (Kaiser, Munarin, and Coulombe 2018) have cast collagen and fibrin hydrogel tissues with laser-etched poly(dimethylsiloxane) (PDMS) molds and demonstrated a cost-efficient way method to create tissue scaffolds. They also pointed out the importance of anisotropy for cardiac regeneration, which could be achieved by designing the microstructure of the composite. This study is a complementary research to Coulombe lab's experimental research(Kaiser et al. 2019) and focuses on the computational modeling of the engineered tissue scaffold. The primary aim of this study is to determine an optimum configuration of the composite from microstructure based finite element analyses.

1.2 Physiology

1.2.1 Heart Structure

The heart lies in the center of the thoracic cavity and is suspended by the attachments to the great vessels within a thin fibrous sac called the pericardium. A small amount of fluid

in the sac lubricates the surface of the heart and allows it to move freely during contraction and relaxation (Mohrman and Heller 2018). The heart consists of two pumps: the left heart pump sends out the blood to the systemic organs, and the right heart pump moves blood through the pulmonary vessels (**Figure 1.1**). The pumping action allows the arterial pressure to be higher than venous pressure so that the blood can flow through all the organs. Each pump is composed of a ventricle and an atrium. The atrium is a weak primer pump that helps to move blood into the ventricle. The ventricle creates the pumping force that propels the blood out.

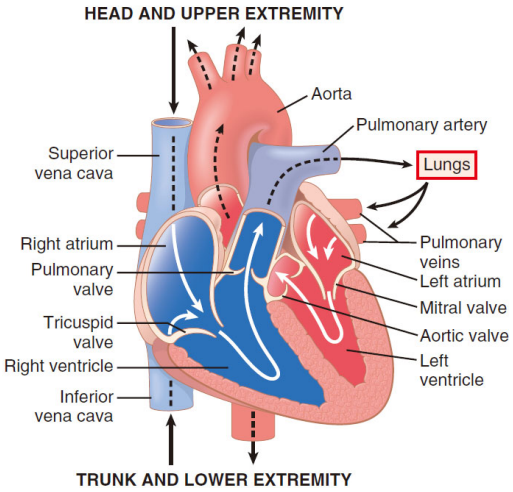

Figure 1.1 Structure of the heart and the course of blood flow through the heart chambers and heart valves (Hall and Guyton 2016)

1.2.2 Cardiac Muscle

1.2.2.1 Histology

The heart is composed of atrial muscle, ventricular muscle, and specialized excitatory and

conductive muscle fibers. The specialized excitatory and conductive muscle fibers contract little as there are few contractile fibrils in them. Their function is to provide an excitatory system that controls the rhythmical beating of the heart. The histology of the cardiac muscle in **Figure 1.2(a)** showed that cardiac muscle is a syncytium of many cardiac muscle cells separated by intercalated discs (the darker area crossing the cardia muscle fibers in the figure). That is, the cardiac muscle fiber is made up of individual cells connected in series, and the muscle tissue is formed by many fibers connected in parallel. This unique structure of cardiac muscle ensures that action potential spreading rapidly.

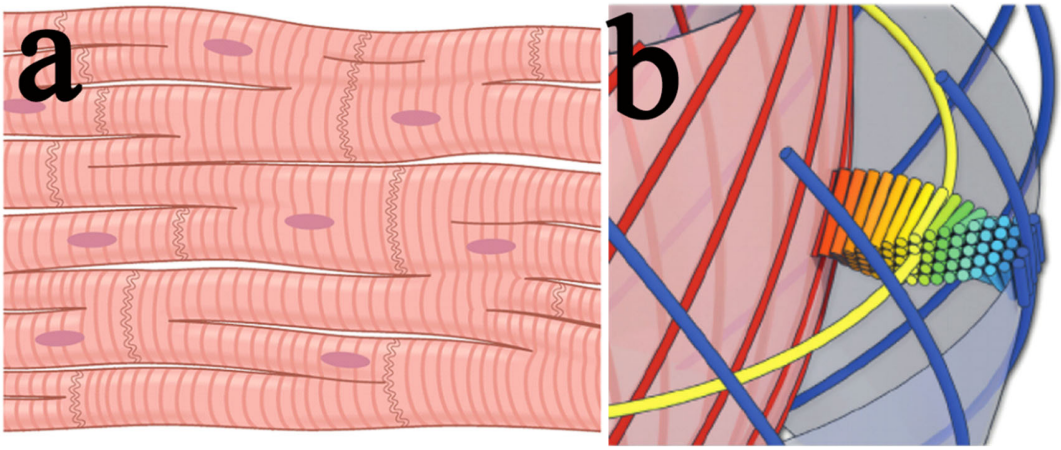

Figure 1.2(a) Histology of cardiac muscle(Hall and Guyton 2016) **(b)**Schematic of muscle fibers across the ventricle wall (Nielles-vallespin et al. 2017)

Ventricular and atrial walls are composed of layers of these paralleled muscle fibers, and the fibers in these paralleled sheets orient differently throughout the ventricle wall. This mural structure results in the anisotropy of the cardiac tissue, which is essential for the propulsion of blood.

1.2.2.2 Constitutive modeling of cardiac tissue

By assuming the passive myocardium to be initially and locally transversely-isotropic, Humphrey et al. determined a constitutive relation for non-contracting myocardium in terms of a pseuostrain-energy function. Holzapfel and Ogden (Holzapfel and Ogden 2009) developed a microstructure inspired orthotropic continuum model for ventricle walls. The angle difference is simplified by taking an average direction as the fiber orientation of the entire tissue. This model is able to describe the shear response in Dokos' experiments(Dokos et al. 2002) and is then used in numerical simulations of post-infarct therapies like left-ventricular assist devices (Bakir et al. 2018).

1.2.3 Cardiac Cycle

The cardiac cycle is defined as the events that occur from the beginning of one heartbeat to the beginning of the next (Hall and Guyton 2016). The cardiac cycle consists of two periods, diastole and systole, in other words, relaxation period and contraction period. As for the blood flow in one cardiac cycle, venous blood from systemic organs enters the right atrium through the inferior and superior vena cava and passes through the tricuspid valve into the right ventricle. This blood is deficient in oxygen; thus, it will then be pumped out to the pulmonary artery through the pulmonic valve. The pulmonary arterial tree is comprised of 17 branch orders, including over 72 million order one capillaries (Townsley 2012), and this is where the "venous" blood being oxygenated. Next, the oxygenated blood flows in pulmonary veins back to the left atrium, through the mitral valve, to the left

ventricle, where the blood is pumped out to the systemic organs. Though the function of the left pump and the right pump is different, the basic pumping behaviors are the same. Take left heart pump as an example, at the beginning of a cardiac cycle, myocardium in the ventricle contracts and creates a tensile force to increase the intra-ventricle pressure, when the ventricular pressure is higher than atrium pressure, the atrioventricular valve closes, and the pressure increases dramatically but is still lower than the blood pressure in the artery. This period is called the isovolumic contraction. After this short period (~0.05s), the ventricular pressure rises rapidly beyond the arterial pressure, and the mitral valve opens, blood flows out to the artery. This is the so-called ejection period and will last for ~0.22 second. After the ejection period, ventricular pressure is slightly lower than arterial pressure; thus, the mitral valve closes (~0.04 second), and diastole begins. At this moment, ventricular pressure is still higher than atrial pressure, so that the atrioventricular valve remains closed until the ventricular pressure becomes lower than the atrial pressure. Compared to the isovolumic contraction period, this period is called the isovolumic relaxation and lasts about 0.08 second. After the atrioventricular valve opens, blood rapidly flows into the ventricle. At the end of the diastole, the atrium starts to contract and presses the rest blood into the ventricle, and is followed by isovolumic contraction, which is the beginning of the next cardiac cycle (Hall and Guyton 2016).(**Figure 1.3**)

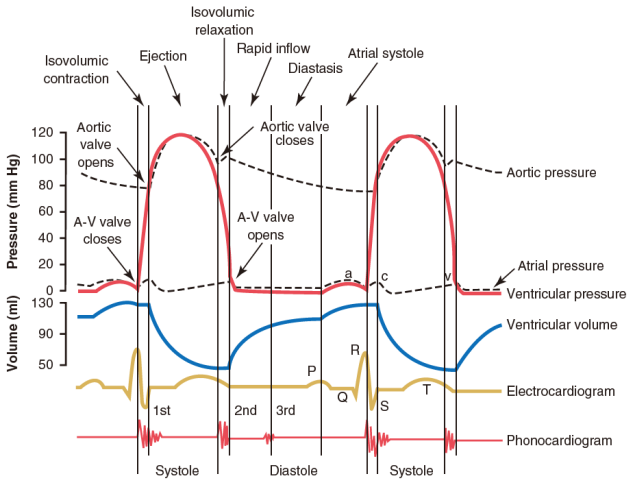

Figure 1.3 Events of the cardiac cycle for left ventricular function(Hall and Guyton 2016)

1.2.4 Myocardial Infarction

1.2.4.1 Acute coronary occlusion

Acute occlusion of a coronary artery is the partial or complete obstruction of blood flow in a coronary artery. It most frequently occurs in a patient who has underlying atherosclerotic coronary heart disease. When the atherosclerotic plaque breaks through the endothelial, its unsmooth surface is then in direct contact with the blood flow. Thus, blood platelets easily adhere to it, and fibrin red blood cells become entrapped to form a blood clot that grows until it blocks the vessel. In some cases, the clot breaks away from the atherosclerotic plaque and flows to a branch of the coronary arterial tree and obstructs that vessel.

1.2.4.2 Myocardial Infarction

As a consequence of an acute coronary occlusion, only a small amount of blood can flow

through the arteries and surrounding vessels. The area of muscle that cannot sustain its function is said to be infarcted. Myocardial infarction occurs immediately after the coronary occlusion. The cardiac muscle cells will die within several hours of little blood supply. Sudden ventricular fibrillation, rupture of the infarcted area, decreased cardiac output, and damming of blood in the pulmonary blood vessels are the most common causes of death after acute myocardial infarction. Among the survivors of myocardial infarctions, postinfarct ventricular remodeling can also lead to congestive heart failure, which can be characterized by progressive ventricular chamber dilatation, wall thinning, and sphericity. Figure 1.4 showed the long-term post-infarct pumping capacity loss due to the initial index event and compensatory mechanisms.

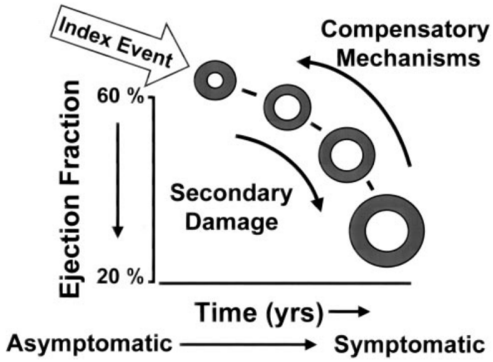

Figure 1.4 Pathogenesis of long-term heart failure(Mann and Bristow 2005)

As the damaged ventricle lacks the capability of ejection because of the infarct area, the heart tends to increase the overall stroke volume to maintain the cardiac output. The stroke volume is defined by

$$\mathrm{SV} = \mathrm{EDV} - \mathrm{ESV}$$

where EDV is the blood volume inside the ventricle at the end of diastole (end-diastolic volume), and ESV is the ventricular volume at the end of systole (end-systole volume). The

way to increase stroke volume is either increase EDV or decrease ESV. Thus, wall thinning and ventricular dilatation are typical characteristics of ventricular remodeling (Mann and Bristow 2005).

1.2.5 Cardiac Patch

In order to reduce secondary damage after myocardial infarctions, regeneration of cardiac muscle is essential in post-infarct therapies. Unlike many other organ systems such as lung, liver, intestine and skin, the mammalian heart is virtually non-regenerative because it does not have sufficient progenitor cells to generate new cardiomyocytes. Implanting exogenous regenerative stem or cardiac progenitor cells is a potential approach to address the problem. However, adult stem cell therapeutic strategies have shown limited benefits to regenerate cardiac function and stop the post-infarct ventricular remodeling. (Pomeroy, Helfer, and Bursac 2019) In 2003, Shimizu et al. developed a three-dimensional scaffold-free graft, which is made up of multiple layers of two-dimensional cell sheets. (Shimizu et al. 2002)This tissue can immediately attach to the heart surface and survive for a relatively long time on infarcted hearts. However, the tissue of cell sheets is so fragile that it cannot withhold its structure even when they are stacked together. In 1997, Eschenhagen et al. have constructed a hydrogel-based cardiac muscle tissue and proved that in vitro isometric contraction is possible. (Eschenhagen et al. 1997) Fujimoto et al. created an elastic, biodegradable cardiac patch and applied it onto subacute infarcted hearts. The patch is improved cardiac remodeling and restored cardiac function after implantation (Fujimoto et al. 2007). Kaiser et al. (Kaiser and Coulombe 2015) pointed out that the design of the

cardiac tissue scaffold should take into account the physiology of heart muscle. That is, the material properties of the engineered tissue, including stiffness, anisotropy and tensile strength is supposed to match that its nearby native cardiac tissue. This can be achieved by designing the microstructure of the scaffold. Kaiser and Coulombe(Kaiser et al. 2019) have designed a fiber-reinforced tissue scaffold in 2019. This scaffold has great potential in its microstructure. It is believed that by designing an optimum configuration of the microstructure, this engineered tissue scaffold can match the material properties of the native cardiac tissue.

1.3 Problem Description

Coulombe's Lab has constructed engineered tissue scaffolds with a hydrogel-based fiber-reinforced composite, which has the potential to be used in cardiac patch applications when the optimum configuration is determined (Kaiser et al. 2019). The tissue scaffolds are composed of collagen microfibers (40 μm diameter) produced with automated wet spinning. These microfibers have a spacing of 200 μm and were embedded in collagen hydrogel bulk with 30° and 60° fiber angles. As the tissue scaffold is not vascularized, it must stay thin so that the cells inside the engineered tissue can obtain nutrients from the nearby area at the implantation site. Consequently, the tissue scaffold is very fragile, so that the composite is only pulled to ~10% strain, which is lower than the regular strain of native heart tissue (20~30% strain). In order to find out the optimum configuration of the engineered tissue, a model that can predict the mechanical response at higher strain is

needed. To meet this gap, the present research study has the following objectives:

a. Create a microstructure-based finite element model of the soft collagen matrix and stiffer collagen microfiber composite tissue scaffold;
b. Conduct a parametric study to understand the effect of design parameters, including fiber angle and the distance between adjacent fibers.
c. Develop a continuum model of the composite tissue scaffold.

Chapter 2. Computational Modeling

2.1 Microstructure based finite element model

2.1.1 Basic steps for finite element analysis

Computational modeling in this study is conducted with the commercial finite element analysis (FEA) software ABAQUS. A typical procedure for finite element analysis is described as follows:

Step 1: Create the geometry of the object structure.

Step 2: Assign material properties to the components in the structure.

Step 3: Generate mesh for the geometry with appropriate types of elements.

Step 4: Define an analysis step and assign proper step size.

Step 5: Apply load and boundary conditions in the analysis step.

Step 6: Run the simulation and post-process.

2.1.2 Creating the geometry

The following procedure is the steps of creating a tensile test specimen geometry that has a fiber angle of 30°. For our initial computational study, we created a set of geometric and loading configurations using 0.08 mm diameter for the microfibers. Note in the Coulombe Lab's experimental study a diameter of 0.04 mm was used for the microfiber (the difference in diameter is due to the misinterpretation of diameter as radius value at the beginning of this study. Our future studies will also incorporate cases for 0.04 mm diameter as well).

The geometric model is created by the preprocessing "Part" Module in ABAQUS with the following steps:

1) Create a solid block part by extrusion with the dimension of $5\,mm \times 3\,mm \times 0.55\,mm$ ($Length \times Width \times Thickness$). (**Figure 2.1(a))**
2) Create the fiber geometry by "Partition." First, create a partition by sketch on the $Width \times Thickness$ face. Note that the fiber cross-section is not a round disk but an ellipsoid as the fiber is cut by an inclined plane. (**Figure 2.1(b)**) The angle between the plane and the fiber is 75°. As a result, the major axis of the ellipsoid is 0.0828 mm, and the minor axis remains 0.0800 mm. Two layers of ellipsoids are tiled across the face. The distance between centers of adjacent ellipsoids in one layer is 0.2070 mm, the distance between centers of adjacent ellipsoids in different layers is 0.100 mm. After creating the partition on the face, use the partition tool by extruding to extend the partitioned face and separate fibers from the block. The extrusion direction is defined using two datum axes that are inclined $\pm 15°$to the longer edge of the composite. (**Figure 2.1(c)**)

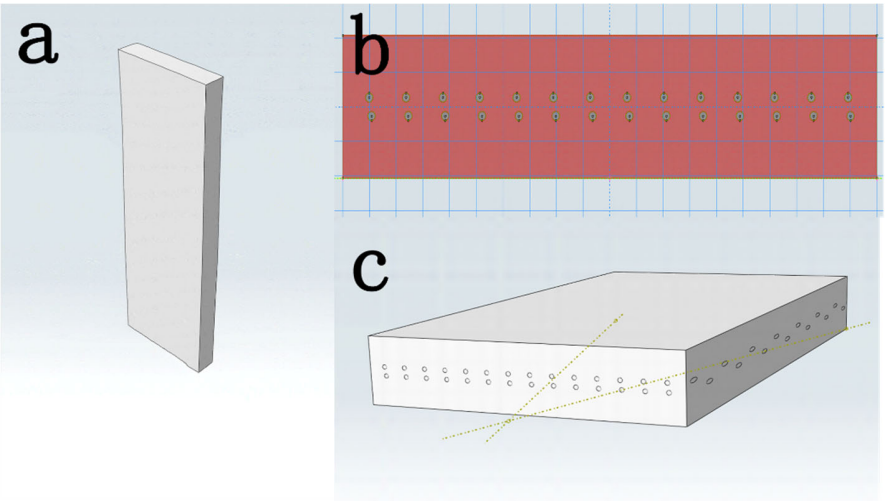

Figure 2.1 Procedure of creating the geometry: (a) Create a solid block; (b) Partition face by sketch; (c) Partition body by extruding

2.1.3 Obtaining material properties of the collagen fiber and matrix

In order to develop this microstructure based finite element model, the material property of each component in this model must be assigned. Two components in this model, fiber and matrix, were tested separately by Coulombe's Lab. We have adopted the Neo-Hookean model for fibers and the Ogden model for matrix by fitting the model material parameters using Coulombe lab's experimental data. The strain energy functions for the Neo-Hookean and Ogden model are

$$\Psi_{Neo-Hookean} = \mu(\lambda_1^2 + \lambda_2^2 + \lambda_3^2 - 3) \quad (2.1)$$

$$\Psi_{Ogden} = \sum_{p=1}^{N} \frac{\mu_p}{\beta_p}(\lambda_1^{\beta_p} + \lambda_2^{\beta_p} + \lambda_3^{\beta_p}) \quad (2.2)$$

Experimental results and fitted Neo-Hookean and Ogden models representing fiber and matrix are presented in **Figure 2.2**. The parameters of these materials are listed in Table

2.1. Due to the misinterpretation of the diameter of the fibers, the stiffness of the fiber in the present research is four times smaller than that in the real case. We will fix this error in future studies.

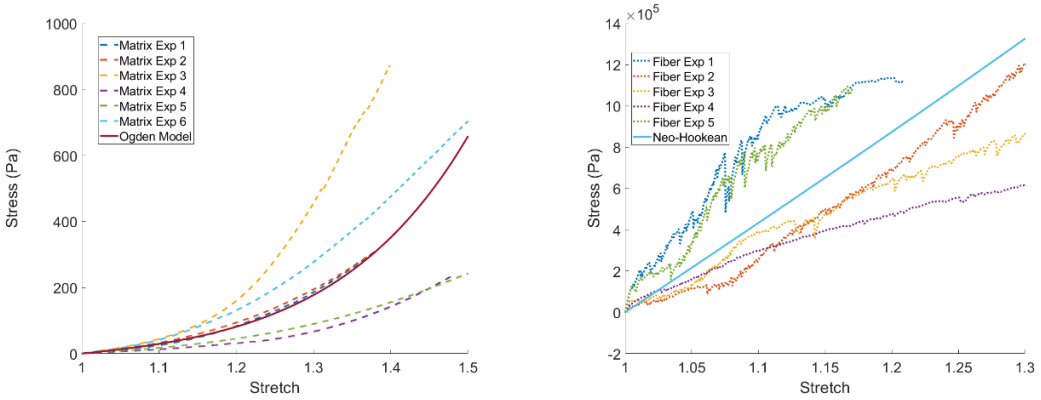

(a) **(b)**

Figure 2.2 Stress-Stretch Results comparing experiments(Kaiser et al. 2019) (dotted curves) with model fits (solid curve). (a) Matrix and (b) Fiber

Fiber	$\mu = 720000$ Pa		
Matrix	$N = 1$	$\mu_1 = 28.4$ Pa	$\beta_1 = 10.42$

Table 2.1 Material parameters for matrix and fiber material

2.1.4 Generate mesh and assign material properties

To obtain a high-quality mesh, the geometry is imported in a commercial software Hypermesh. Hypermesh is a preprocessor for finite element analysis developed by Altair Engineering, Inc. C3D4H, C3D8H hybrid elements are created (**Figure 2.3**) as the composite is considered to be incompressible.

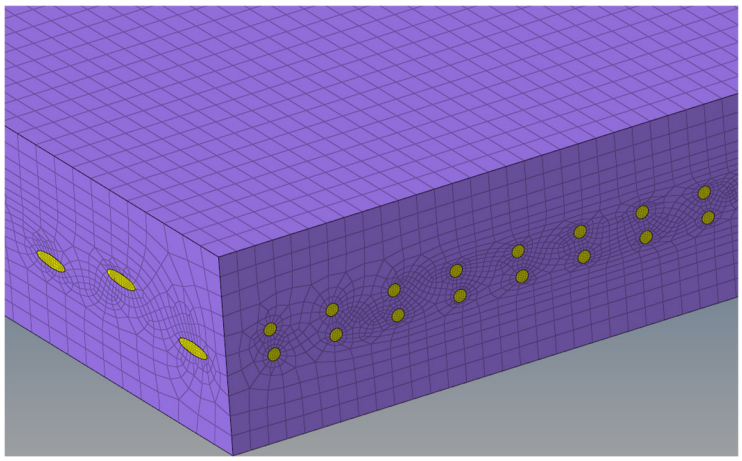

Figure 2.3 Meshed composite in Hypermesh 2019

2.1.5 Apply load and boundary conditions

Import the input file generated in Hypermesh to ABAQUS. In this simulation, the load is applied in the longitudinal direction. For convenience, two node sets, "Top" and "Bottom" are created. In this simulation, the load is applied by setting displacement of the "Top" node set to be 6.5 mm, which is calculated from $\lambda_1 = 1.3$. λ_1 is the stretch in the longitudinal direction. A fixed (Encastre) boundary condition is applied to the "Bottom" node set. The details of the boundary condition are listed in **Table 2.2**.

	U1	U2	U3	UR1	UR2	UR3
Top	-	6.5 mm	-	-	-	-
Bottom	0	0	0	0	0	0

Table 2.2 Boundary conditions for node sets

2.1.6 Results and post analyses

2.1.6.1 Longitudinal Tensile Test

When the composite is stretched in the longitudinal direction, a twisting behavior occurs immediately and gradually slows down as the stretch increases. (**Figure 2.4(a)**) This is probably due to the anisotropic microstructure and the fixed boundary condition at the bottom face of the composite. As shown in **Figure 2.4(b)**, the fibers in one layer remain parallel during the deformation. Fiber distance decreases linearly as the stretch of the composite grows. (**Figure 2.5(a)**). The fiber angle also shows a decreasing trend when the composite is stretched, whereas the relation between angle and stretch formed a nonlinear concave curve, as shown in **Figure 2.5(b)**.

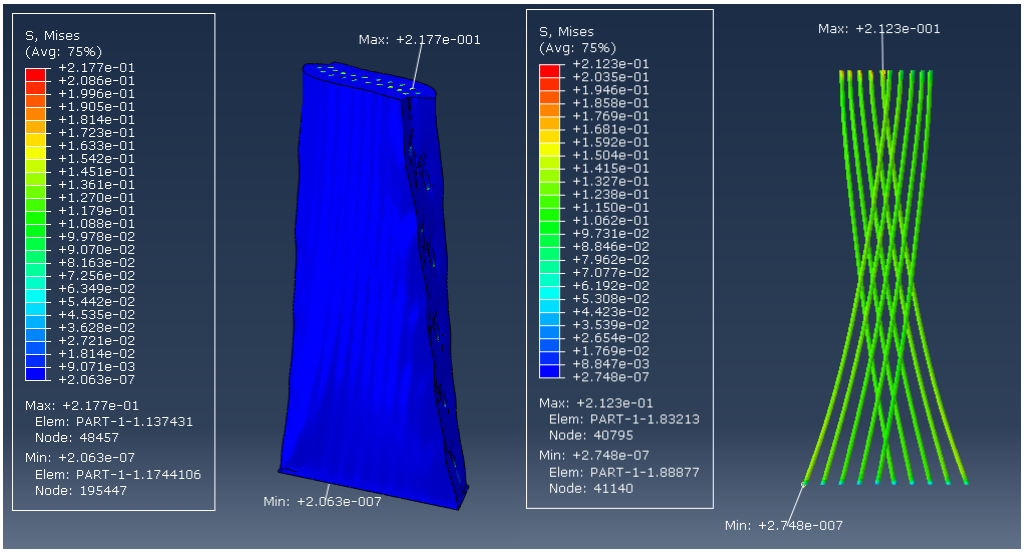

(a) **(b)**

Figure 2.4 Mises stress (MPa) contour plots for longitudinal tensile simulation: (a) deformed composite; (b) deformed fibers

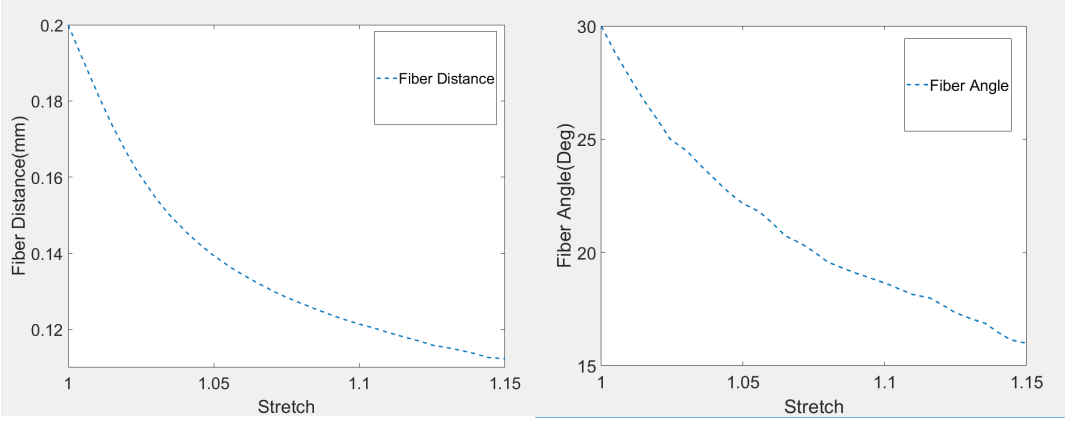

(a) **(b)**

Figure 2.5 Longitudinal direction tensile simulation results (a) Fiber distance vs. composite stretch; (b) Fiber angle vs. composite stretch

2.1.6.2 Transverse Tensile Test

Different from the longitudinal tensile simulation, the twisting behavior is not observed in the transverse tensile simulation. (**Figure 2.6(a)(b)**) In contrast to the longitudinal case, the fiber distance and fiber angle in the transverse tensile simulation both increase in a linear manner with respect to the composite stretch. (**Figure 2.7(a)(b)**).

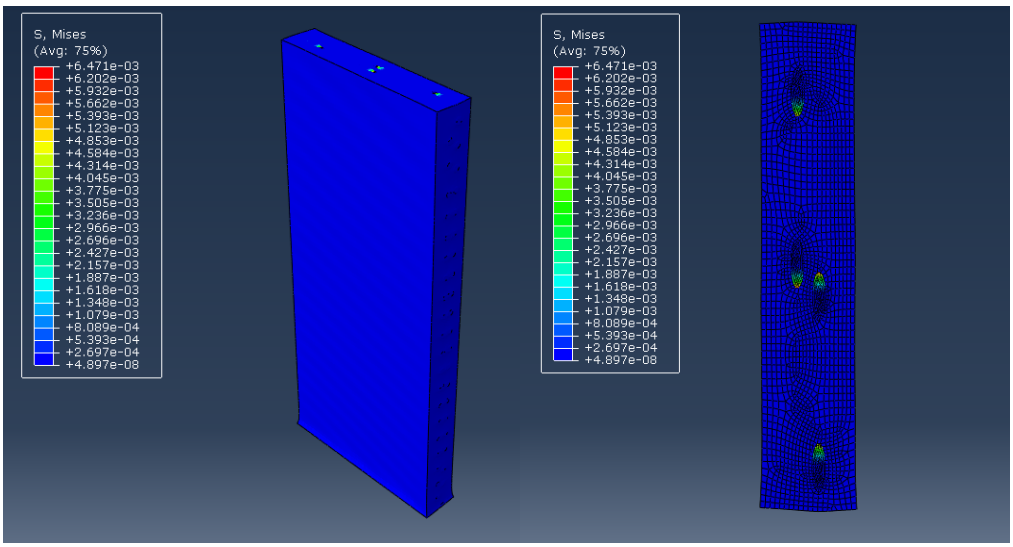

(a) **(b)**

Figure 2.6 Mises stress (MPa) contour plots for transverse direction tensile loading simulation: (a) side view; (b) top view

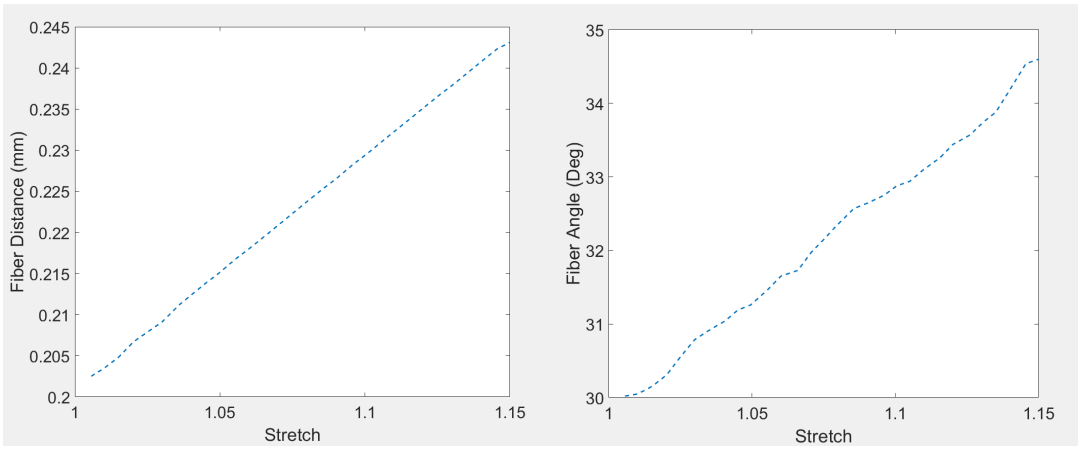

(a) **(b)**

Figure 2.7 Transverse direction tensile simulation results. (a) Fiber distance vs composite stretch; (b) Fiber angle vs composite stretch

2.2 Parametric Study

The simulations in Section 2.1 show that the microstructure-based finite element model can describe the mechanical response of the engineered tissue in both longitudinal and transverse directions. We can now design a parametric study to understand the effects of design parameters of the engineered tissue according to the same methodology as the model described previously. The design parameters of the engineered tissue are fiber distance d_i and fiber angle θ. Values defined for each parameter is listed in Table 2.1. Nine configurations of the engineered tissue are made by pairing every two values as an input. Tensile loading in longitudinal and transverse directions are applied to each configuration.

Fiber distance d_i (μm)	100	150	200
Fiber angle θ (deg)	30	45	60

Table 2.1 Values defined for parametric study

2.2.1 Effect of angle variation

From **Figure 2.8(a)**, the stiffness of the composite is larger when the fibers have smaller fiber angles. This is not surprising because fibers have higher stiffness than the matrix; it is natural to think that the material will be stiffer when the fibers are more oriented. The mechanical response of the composite in the transverse simulation is plotted in **Figure 2.8(b)**. The effect of angle variation is not significant in transverse simulations. By comparing the simulation results with the response of the matrix, we can conclude that the transverse response of the engineered tissue is dominated by matrix.

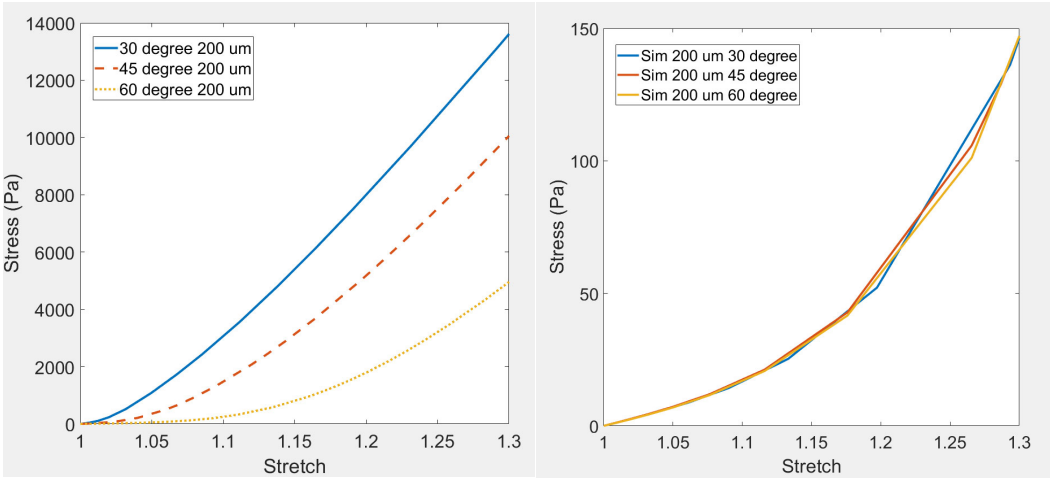

(a) (b)

Figure 2.8 Stress-stretch curves for composites with different fiber angles: (a) longitudinal direction loading; (b) transverse direction loading

2.2.2 Effect of fiber distance

From **Figure 2.9(a)**, it is clear that the composite is stiffer when the fibers are denser in the longitudinal direction. This is due to the higher volume fraction of fiber, which has a larger modulus than the matrix. A similar trend can also be found in the transverse direction, although it is not as evident as it is in the longitudinal direction (**Figure 2.9(b)**).

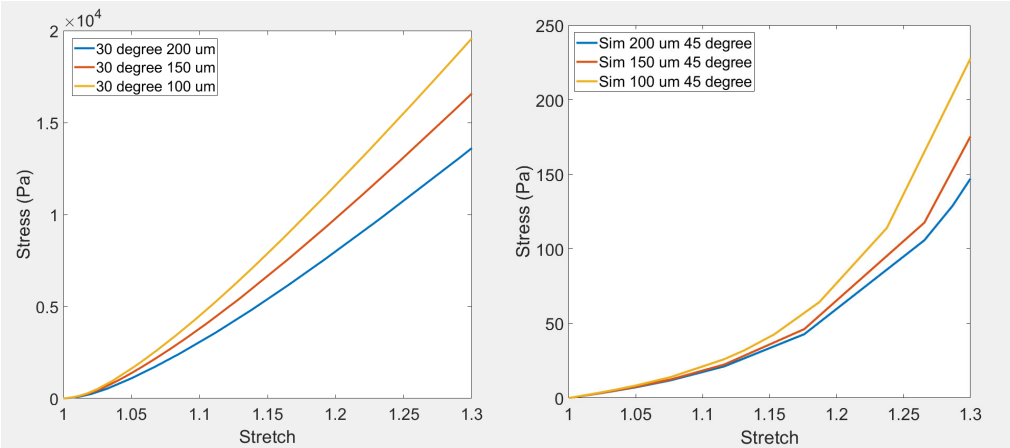

(a) (b)

Figure 2.9 Stress-stretch curves for composites with different fiber distances: (a) longitudinal; (b) transverse

2.2.3 Anisotropy analysis

Among many important material properties of the heart tissue, the anisotropy of the muscle is believed to be important not only in the passive behavior of the material, it also plays a role in the pumping process. The anisotropy ratio is defined as

$$\gamma = \frac{E_L}{E_T}$$

where E_L is the elastic modulus in the longitudinal direction, E_T is the elastic modulus in the transverse direction. Anisotropy ratios of some configurations of the engineered tissue are plotted in **Figure 2.10**. It can be seen that a large fiber angle and distance can result in a relatively low ratio of anisotropy.

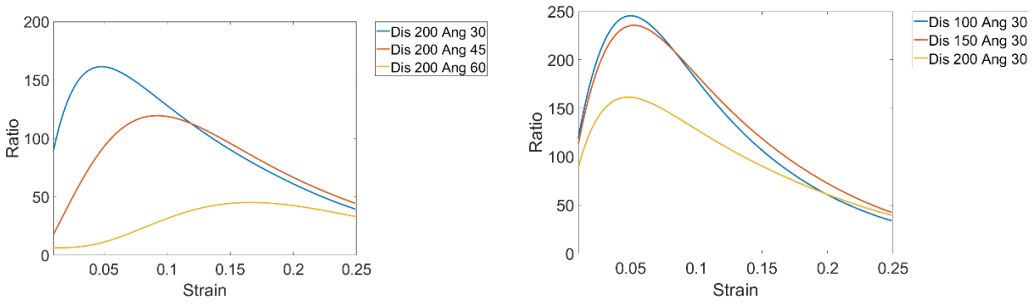

(a) (b)

Figure 2.10 Anisotropy ratios of native cardiac tissue and some configurations of the engineered tissue with the effect of (a) fiber angle difference (b) fiber distance difference.

Chapter 3. Continuum Scale Constitutive modeling

Our next aim is to find out the mechanical response of the heart and the cardiac patch when the patch is implanted on an infarcted heart surface using computational modeling techniques. However, there are several difficulties if we want to follow the microstructure-based modeling we used in Chapter 2:

1) The surface of the heart is not flat; creating the geometry of curving fibers is unrealistic.
2) The microfibers have a diameter of 0.04 mm, whereas the inner diameter of the heart is ~25mm to ~38mm for men. This will result in costly computation.

Thus, we are here proposing a continuum model modified from Holzapfel and Ogden's constitutive model in 2019 (Holzapfel and Ogden 2019).

3.1 Essential elements of continuum mechanics

The primary deformation variable for the local kinematics is the deformation gradient **F**.

The volume change is

$$J = \det \boldsymbol{F} > 0 \tag{3.1}$$

For incompressible materials,

$$J \equiv 1 \tag{3.2}$$

Strain measurements,

Left Cauchy-Green tensor $\boldsymbol{C} = \boldsymbol{F}^{\boldsymbol{T}}\boldsymbol{F}$ (3.3)

Right Cauchy-Green tensor $\boldsymbol{b} = \boldsymbol{F}\boldsymbol{F}^{\boldsymbol{T}}$ (3.4)

Invariants of left Cauchy-Green tensor

$$I_1 = tr\boldsymbol{C} \tag{3.5}$$

$$I_4 = \boldsymbol{M} \cdot \boldsymbol{CM} \tag{3.6}$$

where M is the fiber direction in the reference configuration.

For an incompressible material, the Cauchy stress can be obtained from strain energy Ψ

$$\boldsymbol{\sigma} = \boldsymbol{F}\frac{\partial \Psi}{\partial \boldsymbol{F}} - p\boldsymbol{I} \tag{3.7}$$

It can also be expressed with principle stretches

$$\sigma_i = \lambda_i \frac{\partial \Psi}{\partial \lambda_i} - p \tag{3.8}$$

where, λ_i is the i th principle stretch, and p is the Lagrange multiplier associated with the incompressibility constraint.

3.2 Modification of the Holzapfel model

Holzapfel and Ogden developed a constitutive model to characterize the stiffening effect induced by the density of cross-links in collagenous tissue in 2019. (Holzapfel and Ogden 2019) Although, in the present study, cross-links in the engineered tissue is not considered, we adopted their model with a few modifications. After removing terms of cross-links, we obtained a simplified Holzapfel strain energy function:

$$\Psi = (1 - \Phi)\mu(I_1 - 3) + \Phi\frac{k_1}{2k_2}\{\exp[k_2(I_4 - 1)^2] - 1\} \tag{3.9}$$

where Φ is the volume fraction of the fiber, μ is the shear modulus of the Neo-Hookean matrix, $k_1 > 0$ is a parameter with the dimension of stress, $k_2 > 0$ is a dimensionless parameter.

The limitation of this model is that the material property of the matrix used in this engineered tissue is highly non-linear. Also, the mechanical response of the tissue in the transverse direction is dominated by the matrix, so that it is essential to describe the matrix nonlinearity precisely. The Neo-Hookean model used here clearly cannot meet the requirement. Thus, we decided to use the first order Ogden model(N=1) to describe the isotropic matrix part in the composite. This is also consistent with previous simulations. The model then becomes:

$$\Psi = \frac{(1-\Phi)\mu_1}{\beta_1}(\lambda_1^{\beta_1} + \lambda_2^{\beta_1} + \lambda_3^{\beta_1} - 3) + \Phi\frac{k_1}{2k_2}\{\exp[k_2(I_4 - 1)^2] - 1\} \quad (3.10)$$

In the application of our engineered tissue, the configuration is the same as the first configuration in Holzapfel's paper (Holzapfel and Ogden 2019). (**Figure 3.1**) α is the angle between axial direction and the direction of each family of fibers. (Note: $\alpha = \theta/2$). The direction of the first and second family of fibers is defined as follows:

$$[\mathbf{M}] = [\cos\alpha, \sin\alpha, 0]^T, [\mathbf{M'}] = [\cos\alpha, -\sin\alpha, 0]^T \quad (3.11)$$

Following the assumption made by Holzapfel, the collagen fibers have no out-of-plane component. The fiber directions in the current configuration are denoted by

$$\mathbf{m} = \mathbf{FM}, \mathbf{m}' = \mathbf{FM}' \quad (3.12)$$

$$[\mathbf{m}] = [\lambda_1\cos\alpha, \lambda_2\sin\alpha, 0]^T, [\mathbf{m}'] = [\lambda_1\cos\alpha, -\lambda_2\sin\alpha, 0]^T \quad (3.13)$$

Then we can calculate the invariant I_4

$$I_4 = \mathbf{M}\cdot\mathbf{CM} = \lambda_1^2\cos^2\alpha + \lambda_2^2\sin^2\alpha \quad (3.14)$$

When the material is under uniaxial tension, the principal components of the stress in the

axial and circumferential direction can then be expressed as:

$$\sigma_{11} = 2(1-\Phi)\mu_1\left(\lambda_1^{\beta} - \frac{1}{\lambda_1^{\beta}\lambda_2^{\beta}}\right) + 4\Phi k_1(\lambda_1^2 cos^2\alpha + \lambda_2^2 sin^2\alpha - 1)\exp[k_2(\lambda_1^2 cos^2\alpha + \lambda_2^2 sin^2\alpha - 1)^2]\lambda_1^2\cos^2\alpha - p \quad (3.16)$$

$$\sigma_{22} = 2(1-\Phi)\mu_1\left(\lambda_2^{\beta} - \frac{1}{\lambda_1^{\beta}\lambda_2^{\beta}}\right) + 4\Phi k_1(\lambda_1^2 cos^2\alpha + \lambda_2^2 sin^2\alpha - 1)\exp[k_2(\lambda_1^2 cos^2\alpha + \lambda_2^2 sin^2\alpha - 1)^2]\lambda_2^2\sin^2\alpha - p \quad (3.17)$$

$$\sigma_{33} = 2(1-\Phi)\mu_1\left(\lambda_3^{\beta} - \frac{1}{\lambda_1^{\beta}\lambda_2^{\beta}}\right) - p \quad (3.18)$$

From the uniaxial tension condition,

$$\sigma_{22} = \sigma_{33} = 0 \quad (3.19)$$

Thus,

$$p = 2(1-\Phi)\mu_1\left(\lambda_3^{\beta} - \frac{1}{\lambda_1^{\beta}\lambda_2^{\beta}}\right) \quad (3.20)$$

The stress components in axial and circumferential directions are

$$\sigma_{11} = (1-\Phi)\mu\left(\lambda_1^{\beta} - \frac{1}{\lambda_1^{\beta}\lambda_2^{\beta}}\right) + 4\exp[k_2(\lambda_1^2\cos^2\alpha + \lambda_2^2\sin^2\alpha - 1)^2]k_1\lambda_1^2\Phi\cos\alpha(\lambda_1^2\cos^2\alpha + \lambda_2^2\sin^2\alpha - 1) \quad (3.21)$$

$$\sigma_{22} = (1-\Phi)\mu\left(\lambda_2^{\beta} - \frac{1}{\lambda_1^{\beta}\lambda_2^{\beta}}\right) + 4\,exp[k_2(\lambda_1^2 cos^2\alpha + \lambda_2^2 sin^2\alpha - 1)^2]k_1\lambda_2^2\Phi\,sin\,\alpha(\lambda_1^2 cos^2\alpha + \lambda_2^2 sin^2\alpha - 1) \quad (3.22)$$

The analytical way to obtain the mathematical expression of σ_{11} over λ_1 is to solve $\sigma_{22} = 0$ to get rid of λ_2. By substituting λ_2 with λ_1 in equation 21, we can then get the relation of σ_{11} and λ_1. However, the analytical solution for $\sigma_{22} = 0$ is very hard to find. Because our goal is to create a stress-stretch curve to visually compare with the simulation

results we have and obtain the material parameters for the model, we solve the equation $\sigma_{22} = 0$ numerically at each point of the discretized λ_1. The $\sigma_{11} - \lambda_1$ relation of the model and simulation result is plotted in **Figure 3.2**. The parameters used in this model are shown in **Table 3.1**. Note that as we are using the Ogden model in simulation and constitutive model, it is reasonable to use the same parameters here in the constitutive modeling.

From **Figure 3.2**, the constitutive model predicts the longitudinal response of the composite well at a small stretch($\lambda = 1\sim1.1$) but failed to predict the response precisely at a large stretch($\lambda = 1.25$~1.3). It can be noticed that the mechanical response for the composite becomes more linear when the deformation is large, and the constitutive model presents a nonlinear behavior. This is probably because we used the Neo-Hookean model for the fibers in the simulations, whereas in the constitutive model, we are using an exponential form to represent fiber response. The model cannot predict transverse tensile tests precisely. Both simulation and constitutive models are presenting lower stiffness than the matrix only. A further investigation is needed to understand this behavior.

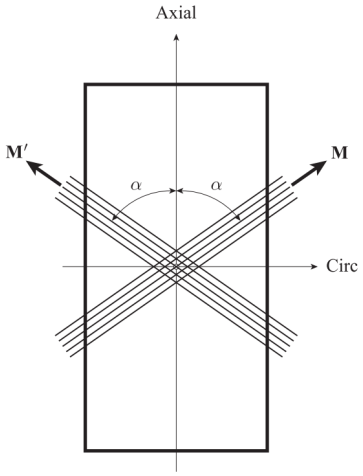

Figure 3.1 Schematic of a rectangular tissue scaffold with two symmetrically arranged families of fibers. (Holzapfel and Ogden 2019)

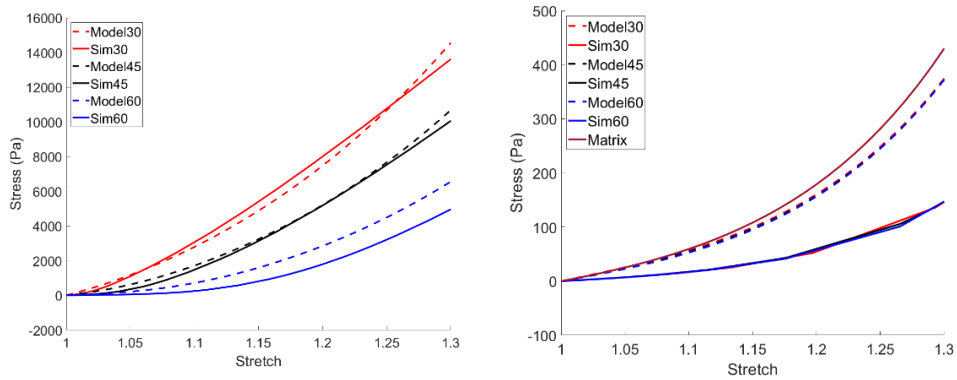

(a) (b)

Figure 3.2 Stress-stretch curve for the proposed model prediction and composite FEA simulation result (a) longitudinal direction loading (b) transverse loading

Φ	μ_1	β_1	k_1	k_2	α
0.0914	28.4 Pa	10.42	29500 Pa	0.1	30°

Table 3.1 Parameters used in the proposed constitutive model

Chapter 4. Conclusion and Discussion

We have developed a set of configurations of engineered tissue scaffold inspired by the experiments from Coulombe's lab. Finite element analysis was conducted for each configuration and predicted the longitudinal and transverse response of the composite. The effects of fiber angle and fiber distance are investigated through sensitivity analysis, including nine configurations and eighteen simulations. The results showed that the longitudinal response is dominated by the fibers at a higher stretch, and the transverse response is determined by matrix. The anisotropy is analyzed in this study, and a large fiber angle and fiber distance will both result in a lower ratio of anisotropy. The finite element simulation capability and its results can aid the optimum design of the engineered tissue.

Based on our simulation results and inspired by works of Holzapfel and Ogden(Holzapfel and Ogden 2019), we developed a continuum orthotropic incompressible constitutive model to describe the mechanical behavior of this composite material. In longitudinal tensile tests, the model fails to predict large strain deformation; this may because we assigned fibers with the Neo-Hookean model, which has a linear relation of stress and stretch. A nonlinear constitutive model will be adopted in the future for the material of fiber in the simulations. In addition, the model here cannot explain the twisting behavior when the composite is loading in the longitudinal direction.

The next step of this study would be application of our continuum orthotropic constitutive model to a simulation with a heart/ventricle like geometry and a cardiac patch. As very simplistic conceptual examples (without a more realistic anisotropic material behavior representation), **Figures 4.1** and **4.2** show simulation results for the case of a damaged heart with a patch and for the case of damaged heart without a patch, respectively. The heart and engineered tissue patch materials in these simulations are simply assumed to be isotropic. A more realistic anisotropic computational model based computational simulations will be performed in the future.

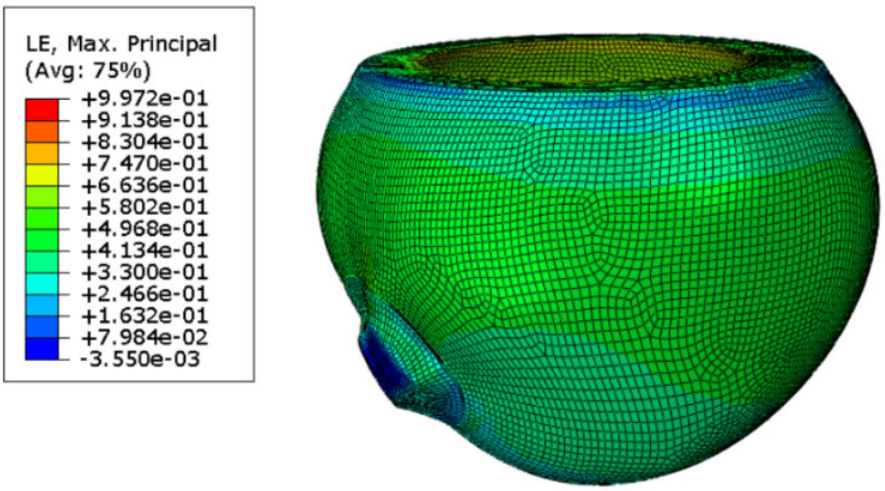

Figure 4.1 Principal strain for the infarcted heart with an implanted patch (finite element simulation assuming isotropic heart tissue and engineered patch)

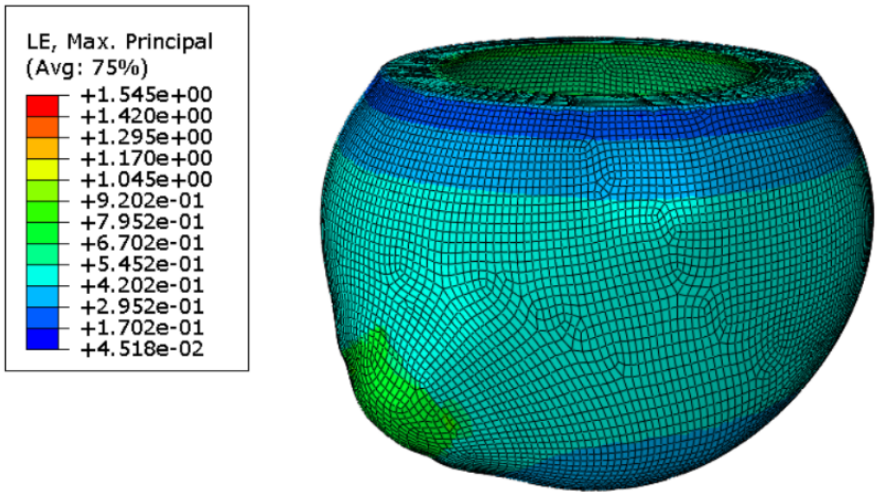

Figure 4.2 Principal strain for the infarcted heart without implanted patch (finite element simulation assuming isotropic heart tissue)

Bibliography

Bahit, M. Cecilia, Ajar Kochar, and Christopher B. Granger. 2018. “Post-Myocardial Infarction Heart Failure.” *JACC: Heart Failure* 6 (3): 179–86. https://doi.org/10.1016/j.jchf.2017.09.015.

Bakir, Azam Ahmad, Amr Al Abed, Michael C Stevens, and Nigel H Lovell. 2018. “A Multiphysics Biventricular Cardiac Model : Simulations With a Left-Ventricular Assist Device” 9 (September): 1–25. https://doi.org/10.3389/fphys.2018.01259.

Dokos, Socrates, Bruce H Smaill, Alistair A Young, I A N J L E Grice, Bruce H Smaill, and Alistair A Young. 2002. “Shear Properties of Passive Ventricular Myocardium,” 2650–59.

Dow, Joan, Boris Z. Simkhovich, Larry Kedes, and Robert A. Kloner. 2005. “Washout of Transplanted Cells from the Heart: A Potential New Hurdle for Cell Transplantation Therapy.” *Cardiovascular Research* 67 (2): 301–7. https://doi.org/10.1016/j.cardiores.2005.04.011.

Eschenhagen, Thomas, Christine Fink, Ute Remmers, Hasso Scholz, Jens Wattchow, Joachim Weil, Wolfram Zimmermann, et al. 1997. “Three-dimensional Reconstitution of Embryonic Cardiomyocytes in a Collagen Matrix: A New Heart Muscle Model System.” *The FASEB Journal* 11 (8): 683–94. https://doi.org/10.1096/fasebj.11.8.9240969.

Fujimoto, Kazuro L, Kimimasa Tobita, § W David Merryman, Jianjun Guan, Nobuo Momoi, Donna B Stolz, Michael S Sacks, Bradley B Keller, William R Wagner, and † § Pittsburgh. 2007. “An Elastic, Biodegradable Cardiac Patch Induces Contractile Smooth Muscle and Improves Cardiac Remodeling and Function in Subacute Myocardial Infarction.”

https://doi.org/10.1016/j.jacc.2007.02.050.

Hall, John E, and Arthur C Guyton. 2016. *Guyton and Hall Textbook of Medical Physiology*. 13th ed. Elsevier.

Holmes, Jeffrey W., Thomas K. Borg, and James W. Covell. 2005. "Structure and Mechanics of Healing Myocardial Infarcts." *Annual Review of Biomedical Engineering* 7 (1): 223–53. https://doi.org/10.1146/annurev.bioeng.7.060804.100453.

Holzapfel, Gerhard A., and Ray W Ogden. 2009. "Constitutive Modelling of Passive Myocardium : A Structurally Based Framework for Material Characterization," 3445–75. https://doi.org/10.1098/rsta.2009.0091.

Holzapfel, Gerhard A, and Ray W Ogden. 2019. "An Arterial Constitutive Model Accounting for Collagen Content and Cross-Linking." *Journal of the Mechanics and Physics of Solids*, no. xxxx: 103682. https://doi.org/10.1016/j.jmps.2019.103682.

Kaiser, Nicholas J., Jessica A. Bellows, Rajeev J. Kant, and Kareen L.K. Coulombe. 2019. "Digital Design and Automated Fabrication of Bespoke Collagen Microfiber Scaffolds." *Tissue Engineering - Part C: Methods* 25 (11): 687–700. https://doi.org/10.1089/ten.tec.2018.0379.

Kaiser, Nicholas J., and Kareen L.K. Coulombe. 2015. "Physiologically Inspired Cardiac Scaffolds for Tailored in Vivo Function and Heart Regeneration." *Biomedical Materials (Bristol)* 10 (3): 34003. https://doi.org/10.1088/1748-6041/10/3/034003.

Kaiser, Nicholas J, Fabiola Munarin, and Kareen L K Coulombe. 2018. "Custom Engineered Tissue Culture Molds from Laser-Etched Masters," no. May: 1–7.

https://doi.org/10.3791/57239.

Mann, Douglas L., and Michael R. Bristow. 2005. “Mechanisms and Models in Heart Failure.” *Circulation* 111 (21): 2837–49. https://doi.org/10.1161/CIRCULATIONAHA.104.500546.

Mohrman, David E, and Lois Jane Heller. 2018. *Cardiovascular Physiology*. 9th ed. New York: McGraw-Hill.

Nielles-vallespin, Sonia, Zohya Khalique, Pedro F Ferreira, Ranil De Silva, Andrew D Scott, Philip Kilner, Laura-ann Mcgill, et al. 2017. “Assessment of Myocardial Microstructural Dynamics b y In Vivo Diffusion Tensor Cardiac Magnetic Resonance” 69 (6).

Pomeroy, Jordan E., Abbigail Helfer, and Nenad Bursac. 2019. “Biomaterializing the Promise of Cardiac Tissue Engineering.” *Biotechnology Advances*, no. November 2018: 0–1. https://doi.org/10.1016/j.biotechadv.2019.02.009.

Shimizu, Tatsuya, Masayuki Yamato, Yuki Isoi, Takumitsu Akutsu, Takeshi Setomaru, Kazuhiko Abe, Akihiko Kikuchi, Mitsuo Umezu, and Teruo Okano. 2002. “Fabrication of Pulsatile Cardiac Tissue Grafts Using a Novel 3-Dimensional Cell Sheet Manipulation Technique and Temperature-Responsive Cell Culture Surfaces.” *Circulation Research* 90 (3). https://doi.org/10.1161/hh0302.105722.

Townsley, Mary I. 2012. “Structure and Composition of Pulmonary Arteries, Capillaries, and Veins.” *Comprehensive Physiology* 2 (1): 675–709. https://doi.org/10.1002/cphy.c100081.

World Health Organizaion. 2018. “World Health Statistics 2018.” Vol. III.